



Charge Optimized Many Body (COMB) potentials for simulation of nuclear fuel and clad[☆]

Simon R. Phillpot^{a,*}, Andrew C. Antony^{a,b}, Linyuan Shi (石临源)^a, Michele L. Fullarton^a, Tao Liang^b, Susan B. Sinnott^b, Yongfeng Zhang^c, S. Bulent Biner^c

^a Department of Materials Science and Engineering, University of Florida, Gainesville, FL 32611, USA

^b Department of Materials Science and Engineering, Pennsylvania State University, University Park, PA 16802, USA

^c Fuels Modeling and Simulation, Idaho National Laboratory, P.O. Box 1625, Idaho Falls, ID 83415, USA

ARTICLE INFO

Article history:

Received 14 October 2017

Received in revised form 14 February 2018

Accepted 17 February 2018

Keywords:

Nuclear materials
Atomistic simulation
Molecular dynamics
UO₂
Zircaloy

ABSTRACT

We briefly outline the Charge Optimized Many Body (COMB) potential formalism, which enables the molecular dynamics simulation of complex materials structures in which multiple types of bonding (metallic, covalent, ionic and secondary bonding) coexist. We illustrate its capabilities to address critical issues in the area of nuclear fuel. In particular, we look at U, UO₂ and the process of oxidation of U. Further, we characterize the mechanical behavior of Zr, representing LWR clad, and explore the effects of oxidation and hydridation on the mechanical response and briefly illustrate the capabilities of COMB simulations of corrosion. Finally, we briefly assess the materials fidelity of the COMB approach by examining the COMB description for the Zr-H system.

© 2018 Published by Elsevier B.V.

1. Introduction

Nuclear fuel is exposed to an aggressive physical, chemical and radiative environment both in operation and in post-use storage. The composition, atomic-level structure and microstructure of both the fuel pellet itself, UO₂ in commercial Light Water Reactors (LWRs), and the clad, usually a Zr alloy, continuously evolve at all length scales from the atomic to the macroscale. All of these changes have significant effects on fuel performance. Current fuel performance codes conflate all of the chemical, physical and microstructural phenomena into a single variable: the burn-up. While these codes, such as FRAPCON [1], have proven very successful in predicting the performance of the UO₂ fuel system, they do have significant limitations. First, their materials models are based on correlations in experimental data; they therefore work well within the domain of performance conditions to which they were fit. However, they are less successful in more extreme conditions. Second, the extensive experimental datasets acquired over decades for UO₂ are not available for other fuel systems. The development of such experimental databases for candidate fuel systems is a significant challenge. There is thus a considerable effort to deconvolve

lute burn-up into its constitutive chemical, physical and microstructural processes, which can then be modeled at the appropriate length scales, thereby enabling the development of more flexible fuel-performance codes. In the United States, the MOOSE-BISON-MARMOT suite of codes are the focus of such development [2].

The atomic-level information for such multiscale fuel performance codes comes from electronic-structure level calculations, typically at the level of density functional theory (DFT), and atomistic methods, most importantly molecular-dynamics (MD) simulation. While DFT generally offers higher materials fidelity, it is limited to small system sizes, almost always less than 1000 atoms. MD is uniquely able to probe nuclear materials with atomic scale resolution and to determine their evolutions over (short) time, including the effects of temperature, stress and radiation. In MD, atoms are generally treated as indivisible, structureless objects, interacting with each other through empirical potentials which describe the interatomic forces between atoms. These potentials do not explicitly describe the electrons; rather, they attempt to incorporate all of the complex effects of the interacting electrons in the form of a functional form and/or numerical tables. Because they do not describe the electrons explicitly, simulations using empirical potentials are orders of magnitude faster than their DFT counterparts.

[☆] This article belongs to the special issue : Radiation Effects

* Corresponding author.

E-mail address: sphil@mse.ufl.edu (S.R. Phillpot).

There are well-known and very successful interatomic descriptions for the description of various classes of materials: embedded atom methods (EAM) and modified embedded atom method (MEAM) potentials for metals; bond order and many-body potentials for covalent materials; Coulomb potentials plus empirical short ranged potentials, such as Buckingham potentials, for ionic systems. However, it is only in the last few years that methods have been developed that allow the description of systems in which different types of bonding co-exist [3]. Such systems are endemic in nuclear materials. For example, oxide fuel can develop metallic fission product clusters; the oxide fuel and fission products can react chemically with the clad. Moreover, the clad is subject to oxidation and hydriding in the aggressive reactor environment.

In this paper, we discuss briefly the Charge Optimized Many Body (COMB) formalism, which is one particular type of interatomic potential capable of describing the different types of bonding in an integrated manner. We illustrate the capabilities of COMB for attacking various problems of interest in the area of nuclear fuels. The coverage of each area is perforce brief. The interested reader will be guided to the original papers throughout. While this review focuses on the COMB approach, it is important to note that there is a very extensive literature on the simulation of fuel systems, most particularly UO₂ using atomistic techniques.

The rest of this review is organized as follows. In Section 2, we briefly introduce the COMB formalism and identify the systems, both nuclear and non-nuclear, that have already been parameterized. In Section 3, we look at U, UO₂ and the process of oxidation of U. In Section 4, we look at the mechanical behavior of Zr, representing LWR clad, and explore the effects of oxidation and hydridation on the mechanical response. In Section 5, we describe the capabilities of COMB simulations of corrosion. Since there has been relatively little work done in this area, we also describe some work performed on non-nuclear materials, which illustrate the capabilities of COMB. Section 6 briefly describes some of the known limitations of the COMB approach. Section 7 contains our conclusions and identifies future research directions.

2. COMB formalism

Metallic bonding is characterized by the near uniform background of electrons shared among all of the atoms. By contrast, covalent bonding involves the sharing of electrons between two atoms, while ionic bonding involves the transfer of electrons from one atom to another. DFT methods show these differences clearly. While classical empirical potentials used in MD simulations do not explicitly describe the electrons, they do include surrogate quantities that account for the effects of electrons on bonding. For examples, the central concept of the EAM approach is a density function which, while determined from the positions of neighboring atoms, purports to describe the local density of the background electrons. Potentials typically capture covalency through a bond-order term, which modulates the strength of a bond between two atoms based on the number and nearness of their neighbors. Interestingly, it has been shown that there is a fundamental equivalence between the EAM approach and the bond-order approach [4]. Similarly, in descriptions of ionic materials, the effects of electron transfer between atoms are captured by the charges on the ions, which interact with each other through Coulombic interactions.

The COMB potential approach combines the ideas of bond order (aka electron density) and variable ionic charge to produce a flexible interatomic description of all three types of bonding [5–7]. Specifically, the charge on each atom is not fixed in COMB, but changes according to its local environment; for example, a Si atom in bulk silicon is charge neutral, while a Si atom in SiO₂ is positively

charged. Moreover, the charge is not imposed on an atom but is determined autonomously on the fly during the simulation and changes as the local structural and chemical environment changes. While this paper focuses on the COMB potential, it shares many common features with the ReaxFF [8] approach [6,7].

COMB is straightforward in concept, in that it combines a bond-order approach with a charge equilibration methodology, which enables the charge on an atom to adjust autonomously, and in a self-consistent manner. In schematic form, the total energy function describing the COMB potential, E^{COMB} , can be written as

$$E^{\text{COMB}} = E^{\text{self}} + E^{\text{Coul}} + E^{\text{polar}} + E^{\text{vdw}} + E^{\text{bond}} + E^{\text{other}} \quad (1)$$

Here E^{self} is the energy associated with the ionization of an atom, E^{Coul} is the Coulombic interaction between ions, E^{polar} is the dipole and higher order electrostatic interactions, E^{vdw} is the van de Waals interactions, E^{bond} is the bond-order energy and E^{other} is used to describe very specific bond angle configurations. Each of these terms is written as a functional form depending on the charges $q = \{q_1, q_2, \dots, q_N\}$ of the N atoms/ions in the system their positions $\mathbf{r} = \{\mathbf{r}_1, \mathbf{r}_2, \dots, \mathbf{r}_N\}$. The full details of the COMB formalism are discussed in detail elsewhere [6]. Here we just highlight the key points that enable the description of all bonding types in a single formalism.

The key term involved in the self-consistent charge equilibration is the self-energy, which can be written as:

$$E^{\text{self}} = \sum_{i=1}^N \chi_i q_i + 1/2 J_i q_i^2$$

Here χ_i is the electronegativity of species i and J_i is the chemical hardness; higher order terms can also be included. The self-energy term imposes a relative difference in energy cost for various charge states of a particular element. For example, we would expect oxygen to have zero charge in a covalent system and be negatively charged in an oxide, while a metallic atom such as Cu would be neutral in the metal and positively charged in an oxide. This is captured in the very different values of χ and J for O and Cu. The most important charge dependent terms are the Coulombic interactions and the bond order terms. The interested reader is referred to more detailed discussions [6].

The charge and position of each atom can be determined using a charge equilibration (Qeq) method [9] within an extended Lagrangian formalism:

$$L = \sum_{i=1}^N \frac{1}{2} m_i \dot{r}_i^2 + \sum_{i=1}^N \frac{1}{2} M_Q \dot{q}_i^2 - E^{\text{COMB}} - \lambda_L \sum_{i=1}^N q_i. \quad (2)$$

In Eq. (2), the first term is the kinetic energy associated with the physical movement of the ions, where m_i is the atomic mass of species i . The second term is the kinetic energy of the charges with a fictitious charge mass (M_Q), and λ_L is an undetermined multiplier that forces the charge in the system to be conserved. The incorporation of a fictitious charge mass is equivalent to the inclusion of a piston mass in the Andersen and Car-Parrinello barostats: it is an inertia and simply sets the timescale over which the charge of the system can adjust to equilibrium.

The Lagrangian can be analyzed in the usual manner to determine the equations of motion (EOMs) for the charge and the position of each atom. The EOM for the position is the standard Newtonian equation for the evolution of atomic positions. The EOM for the charge shows how the charge evolves in a coupled manner with the evolution of the atomic positions.

Although it is structurally quite simple, the current, third-generation COMB implementation, COMB3, has a large number of terms, required to describe various physical and chemical phenomena. As a result, it has a large number of parameters, many tens for

a binary system. The parameterization of these potentials is therefore a time-consuming and difficult process. Advances in parameterization methods have been made, but further progress is greatly needed. All of the COMB3 parameterizations are consistent such that they can, at least in principle, be used together. However, not all of the cross terms have yet been determined. Table 1 gives a list of the systems for which COMB3 parameterizations have been developed. COMB3 is distributed in LAMMPS.

There are also potentials in the first (COMB1) and second-generation (COMB2) formalisms for Si-SiO₂ [10–12]; Cu-SiO₂ [13,14]; Cu-Cu₂O [15] and Hf-HfO₂ [16]. These are however now obsolete.

The complexity of the COMB formalism and the multiple charge equilibration steps at each MD step results in it being computationally expensive: when full charge equilibration is included, about 100 times more expensive than EAM. This is very similar to the speed of ReaxFF.

In the next sections, we illustrate how MD with COMB potentials enables us to address a number of important questions relevant to nuclear materials.

3. Application of COMB to U and UO₂

UO₂ fuel in Zr alloy clad is the fuel system in all commercial reactors in the US and widely used elsewhere in Light Water Reactors (LWRs). There has also long been interest in U alloys as a metallic fuel.

3.1. Uranium

Under ambient conditions U has an orthorhombic structure, unique among the elements. Until quite recently, there were no classical interatomic potentials available for U metal at all. This changed in 2012, with the publication of four potentials in a short period of time. Two of these potentials are conventional EAM potentials [37,38], one uses a newly developed long-range (LR) potential formalism [39], the fourth was a COMB3 potential [21]. A MEAM potential has also been developed [40]. A second higher-fidelity COMB3 potential has been developed more recently [23]. Fig. 1 shows the deviation from experimental values of the cohesive energy, various structural parameters and elastic properties predicted by these U potentials and by DFT at the level of the Generalized Gradient Approximation (GGA). The structural parameters, including γ , which characterizes the internal atomic coordinate of the U atoms in the orthorhombic structure, are reproduced with high accuracy by all of the potentials. By contrast, the elastic constants are less well reproduced. The potentials particularly struggle to reproduce the c_{44} shear constant; this is not unexpected as even for more symmetric materials the shear constant(s) are often the most difficult to reproduce. In fitting our COMB potentials, we use experimental values where available and values from DFT calculations when experimental values are not available.

The COMB potential gives an ionization energy (IE) of uranium of 6.08 eV, which is very close to the experimental value of 6.05 eV [41]. The only defect formation energy of α -U that is known experimentally is that of the vacancy (1.5 eV) [42]. DFT calculations are reasonably consistent with this, with two different studies giving values of 1.7 eV [21] and 1.95 eV [43]. For consistency with other defect calculations, for which experimental target values are not available, the COMB potential was fit to the DFT value of 1.7 eV. The resulting COMB value is 1.9 eV, which is similar to that of the Smirnova EAM potential (2.0 eV) [37]. COMB underpredicts the formation energies of the I4 and I5 interstitials in α -U compared with DFT, leading to an underestimate in the Frenkel energy (4.5 vs. 6.0 eV).

Table 1
COMB3 potential parameterizations.

Cu–ZnO	[17,18]
C–O–H–Cu	[19,20]
U–O ₂ –UO ₂	[21–23]
Ti–TiO ₂ –TiN	[24,25]
Ti–TiC	[26]
Zr–ZrO ₂ –ZrHx	[27–29]
Ni–Al	[30,31]
Cu–H ₂ O	[32]
Al–Al ₂ O ₃ –AlN	[33,34]
Pt	[35]
Au	[35]
N–C–O–H	[36]

The COMB3 potential predicts the structure and elastic properties of tetragonal β -U quite well (e.g., $B = 120$ vs. 132 GPa) even though this phase was not part of the fitting database. The structure of bcc γ -U is well reproduced by the COMB3 potential, while the elastic properties and defect energies match DFT values with varying degrees of accuracy [23].

A potential with reasonable physical fidelity opens up a large number of opportunities for structural analysis. For example, Fig. 2 shows the formation of a prismatic dislocation loop, produced by the structural organization of initially randomly located Frenkel pairs in α -U; such Frenkel pairs, though injected into the simulation by hand, mimic the effects of radiation damage to pure U.

3.2. Uranium dioxide

As the dominant fuel material, there are a large number of interatomic potentials for UO₂. The predictions for various structures and properties of many of these have been analyzed in detail by Govers et al. [44,45]. The phase stability and thermal transport properties of 26 UO₂ potentials, including many of the same characterized by Govers, have been determined by Chernatynskiy et al. [46]. All of these potentials prescribe the ionic charges on the uranium and oxygen and constrain $q_U = -2q_O$; they are thus limited in applicability to UO₂ and cannot describe other oxides such as U₃O₈ or U₄O₉, since they would not be charge neutral with these potentials. A tight-binding variable charge mode (SMTB-Q) well describes the properties of bulk UO₂ and its surfaces [47].

During its life-cycle, both in reactor and after removal, the composition and microstructure of UO₂ fuel evolve dramatically. In particular, fission products are continuously produced and they can be in the form of gases such as Kr and Xe, in the form of metallic inclusions such as Mo and Ru, and as oxides such as Y, Zr and Nb [48].

All of the potentials reviewed in the above papers have functional forms that are well-adapted for looking at largely ionic systems such as UO₂. They have also been used with considerable success to explore the effects of gaseous fission products. Indeed, if one is interested in pure UO₂ alone, then a traditional ionic potential is quite possibly the best choice because each ionic potential parameterization usually endeavors only to describe one or a few closely related materials; they may thus be able to provide a high level of materials fidelity, despite their simplicity. This simplicity in these fixed-charge potential formalisms means that they are also much more computationally efficient than variable charge formalisms such as COMB. However, they have not generally been parameterized for other largely ionic fission products. Moreover, they cannot be used to describe metallic fission products or the fuel-clad chemical interactions.

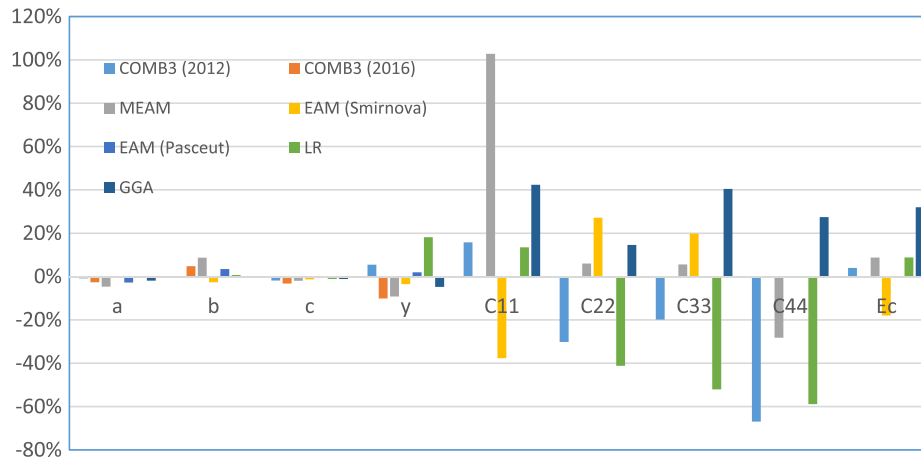


Fig. 1. Percentage error in representative structural and elastic properties of α -U calculated in various potentials and from DFT calculations using GGA, compared with experiment. Constructed from data in [23].

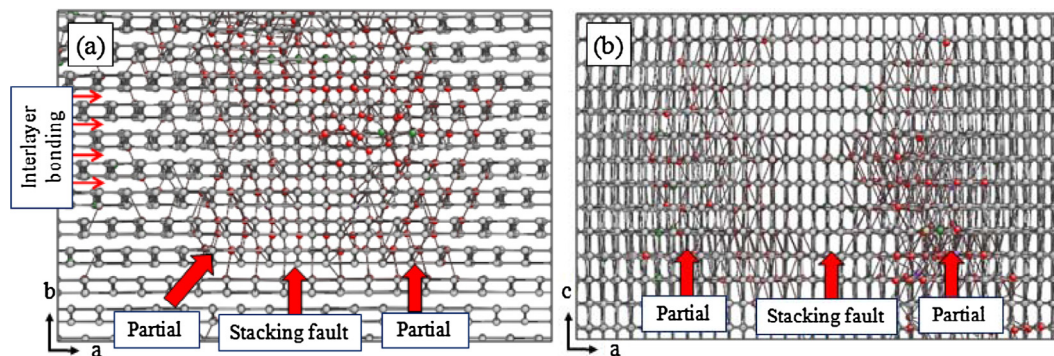


Fig. 2. Extended dislocation loop with Burgers vector $b = [1\ 0\ 0]$ from a COMB simulation of α -U. Views along the (a) c axis and (b) b axis with all atoms shown. The partial dislocations and stacking fault are identified [23].

Reactive potentials such as COMB are able to describe all types of bonding simultaneously. As a first step to an integrated set of potentials for fuel and fission products, we have developed a COMB potential for the U-UO₂-O₂ system [21–23].

In fitting the COMB potential for the U-O system, it was also necessary to consider oxygen atoms and molecules. The COMB potential yields an oxygen ionization energy of 13.31 eV, compared with the experimental value of 13.6 eV and an electron affinity of 1.40 eV, compared to the experimental value of 1.46 eV [22]. The COMB potential also yields an O–O bond length of 1.21 Å, identical to the experimental value and a cohesive energy of –2.58 eV, which compares well to the experimental value of –2.56 eV.

To illustrate COMB’s capabilities for describing both metallic and ionic bonding, we have examined the oxidation of uranium, which involves a change in bonding type from metallic to ionic.

Fig. 3(a) shows the initial structure of α -U with two oxygen interstitial added (uranium atoms are red; oxygen atoms green¹), which is essentially identical in DFT and MD; initially the nearest-neighbor oxygen distances are 2.04 Å in DFT and 2.05 Å in COMB. Fig. 3(b) and (c) show the final relaxed structures obtained from DFT and MD. They show the lengths of the six initially identical U–O bond distances into three pairs of clearly different lengths: 2.43, 2.32 and 2.04 Å for DFT and 2.52, 2.38 and 1.93 Å for COMB. This illustrates the capability of the COMB potential to reproduce the DFT results with, at least, semi-quantitative accuracy. In the

COMB simulation, the oxygen atoms take on a negative charge, while the nearby uranium atoms take on a positive charge, indicative of a change in bonding type from metallic to ionic.

The defect energies associated with an O atom in U match the DFT values reasonably well, –4.3 eV COMB vs. –3.3 eV DFT, for the four-coordinated (I4) site and –4.3 eV vs. –4.1 eV for the five-coordinated (I5) site. COMB predicts higher stability of the O₂ molecule than DFT, –6.4 eV vs –3.8 eV for the I4 site and –6.0 eV vs. –3.4 eV for the I5 site [22].

To carry this example further, we have looked at the effect of adding a high concentration of oxygen interstitials to α -U; although this is not a physically realizable scenario, it illustrates the power of the COMB approach. As Fig. 4 shows, the introduction of the oxygen into the orthorhombic U lattice results in the development of domains of fluorite-structured UO₂. Due to the symmetry of the α -U and of the fluorite structure, it is possible for the fluorite to form in distinct orientations. These oxidation effects cannot be simulated with the traditional potentials used for metallic, covalent and ionic systems.

4. Mechanical properties of Zr-based clad

The COMB potential for the Zr-O-H system [27,28] was developed to allow the elucidation of the mechanical properties of these systems and the corrosion properties of Zr (see next section). Together with the U-O₂-UO₂ potential, it also forms the foundation of a future integrated potential for fuel, clad and fission products. We illustrate the capabilities of this potential for mechanics by

¹ For interpretation of color in Fig. 3, the reader is referred to the web version of this article.

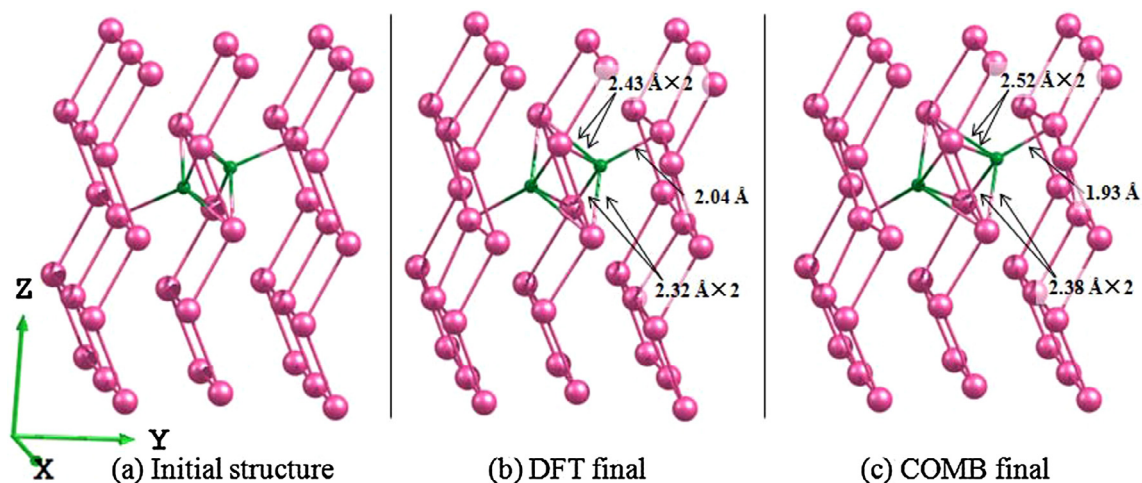


Fig. 3. Structural relaxation of an oxygen molecule at the 15 site in α -U simulated by (b) DFT and (c) COMB; (a) is the initial structure of both DFT and COMB. The lengths of U–O bonds surrounding one of the O atoms in each method are labeled. From Li et al. [21].

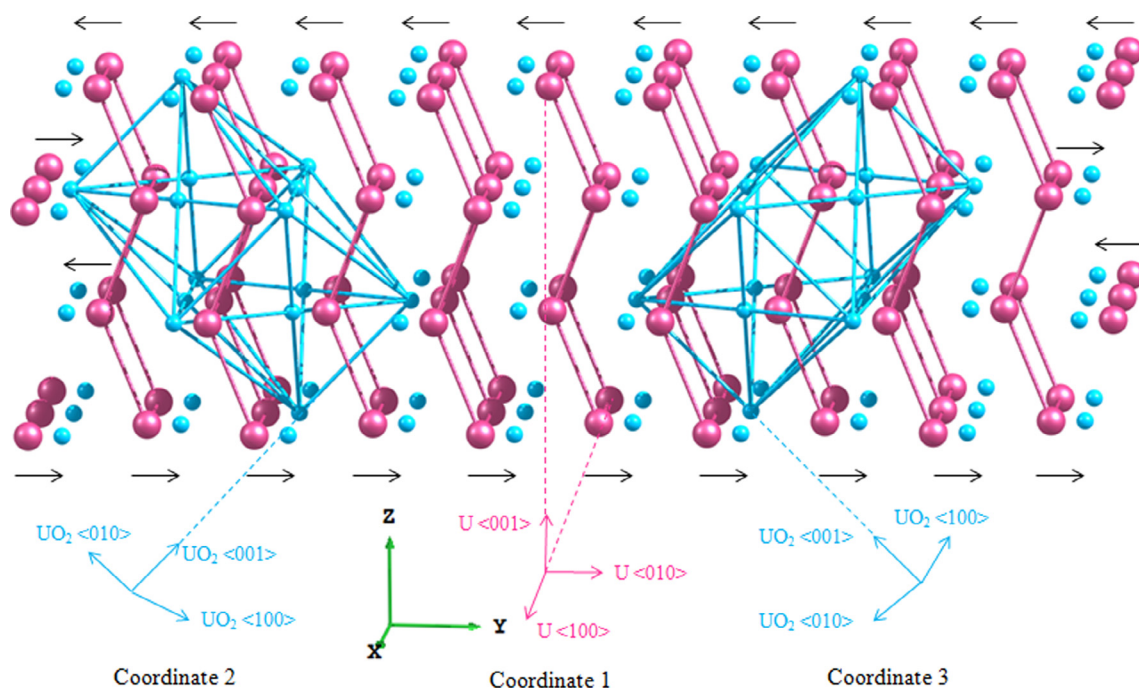


Fig. 4. The orientation relation between the orthorhombic α -U and fluorite UO_2 . Large, purple atoms are U atoms in original α -U structure under Coordinate 1. As the transformation starts, they move in (0 1 0) direction indicated by black arrow to become small, cyan atoms. The cyan atoms form a pseudo-fcc lattice under Coordinate 2 or 3. From Li et al. [21].

looking at nanoindentation of a ZrO_2 overlayer on a Zr substrate and of ZrH_x .

The ZrO_2 overlayer on Zr represents oxidized clad. We were interested in elucidating the mechanical behavior of such a system, in particular the differing deformation modes in the brittle ionic overlayer and the more ductile metallic substrate. The deformed structure during the nanoindentation simulation (with oxygen atoms removed from the image for clarity) is illustrated in Fig. 5. To identify defects in the crystal structure, common neighbor analysis (CNA) [49,50] is applied separately in Zr and ZrO_2 to identify fcc-like atoms, hcp-like atoms and disordered atoms. Dislocation extraction analysis (DXA) is then used to identify dislocation lines. All other atoms are omitted from the figures. The upper red line of atoms lies at the top surface of the ZrO_2 layers, while the lower line lies at the ZrO_2 /Zr interface; the oxide

layer is 36 Å thick. As illustrated in Fig. 5(a), pyramidal dislocations start to nucleate in the Zr substrate at an indentation of ~ 12 Å. The dislocation lines in the top ZrO_2 layer are captured by DXA at an indentation depth of 18.5 Å as shown in Fig. 5(b). The green dislocation line in Fig. 5(b) is a $1/6 \langle 110 \rangle$ Shockley partial, while the Burgers vector of the red dislocation cannot be identified by the DXA. Before the formation of dislocations in ZrO_2 at around 18 Å, the ZrO_2 layer deforms the system along the $[110]$ direction. Load-indentation curves allow us to determine the hardness, which fluctuates over a narrow range between 13 Å and 18 Å; this is similar to the pure Zr case [51]. The hardness starts to decrease after 18 Å where the load starts to drop and the dislocations start to form in the ZrO_2 layer. When we indent deeper than 24 Å, the ZrO_2 /Zr system fails and the ZrO_2 fragments in an explosive manner as it is not able to absorb more

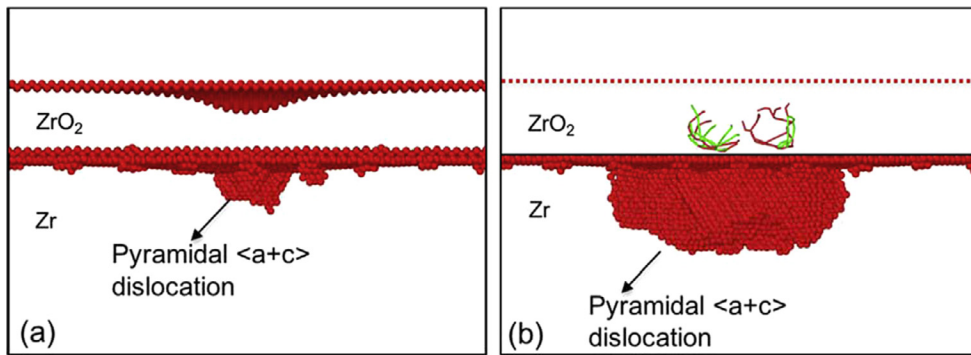


Fig. 5. Deformed structure of ZrO_2/Zr system after nanoindentation. (a) Deformed structure at 12.4 Å indentation depth. The red atoms represent disordered atoms. Atoms in fcc and hcp environment have been removed. (b) Deformed structure at 19 Å indentation depth. The atoms in ZrO_2 layer have been removed. Only dislocation lines are shown. Green lines represent the Shockley partials. Red lines represent other dislocations types. The dislocation lines are captured using DXA. From Lu [52]. (For interpretation of the references to colour in this figure legend, the reader is referred to the web version of this article.)

energy. This failure of the ZrO_2 is likely the result of the thinness of the oxide layer.

Zr clad can react with water to form hydrides of various compositions. The processes of hydride formation and the mechanical properties of the hydride are also of considerable interest because the hydride can have a considerable effect on the mechanical performance of clad. Specifically, hydrides are brittle and they severely degrade the integrity of fuel pins by reducing the overall fracture toughness [53,54]. To characterize its mechanical properties, we performed nanoindentation simulation on the charge-neutral (1 1 0) surface of ZrH_2 using the Zr-H COMB potential [28]. Similar to the case of ZrO_2 , load-displacement curves for various indentation speeds and active layer thicknesses were determined, as shown in Fig. 6(a). There is no significant difference between the load-displacement curves for different indenter speeds, demonstrating that indenter speed has a limited impact on the simulation. As we also saw in similar studies of ZrO_2 , there is a slight dependence on the thickness of the nanoindented layer (62 Å vs. 109 Å). The theoretical load-displacement curve according to Hertz law is indicated by the red line and it can be seen that all curves follow the trend of Hertz law, with the 109 Å layer matching it very closely up to 16 Å indentation depth. At this depth, the first plastic deformation begins and defect structures are generated causing the load-displacement curve to deviate from Hertz law.

The atomic-level details of plastic deformation in the process are analyzed for the whole system with an indentation depth of 16 Å. No dislocations are observed using CNA, so the centrosymmetry (CS) parameter [55] is used to measure the degree of atom disorder. The CS parameter represents symmetry, a lower CS values means lower asymmetry and the CS parameter for an atom in a perfect lattice is zero. Surface atoms have a large positive CS parameter. Fig. 6(b) shows the Zr atoms with a CS value greater than 3, that is those with high asymmetry and therefore disorder, and with H atoms removed.

Fig. 6(b) shows two dislocation loops along $\langle 110 \rangle$ directions forming during the loading process. DXA analysis is used to identify the dislocation types. The dislocations along the $1/2 \langle 100 \rangle$ directions gradually nucleate as plastic deformation begins at approximately 16 Å indentation depth, coinciding with a small decrease in hardness. The disorder associated with the dislocations decreases as they slip or are annihilated by another dislocation from the opposite direction until an indentation depth of 17 Å, at which the dislocations disappear. The hardness increases between 17 Å and 20 Å, at which point the $1/2 \langle 100 \rangle$ dislocations and $1/6 \langle 110 \rangle$ Shockley partial dislocations reappear. With the reappearance of dislocations, additional force is not required to indent deeper, thus, the slope of load-depth curve decreases and the force

applied and material hardness remain steady between a 20 Å and 25 Å indentation depth.

The above analyses illustrate the capability of COMB to elucidate the mechanical properties of Zr-ZrO_2 and ZrH_2 . In the future, it will be very interesting to look at clad configuration in which both the oxide and hydride are present.

5. Simulation of first stages of corrosion with COMB

Both the clad and many of the structural metals in reactors are in contact with water at high temperature and pressure. They are thus subject to corrosion. We first illustrate the ability of the COMB potential approach to simulate the reactions of H_2 , O_2 and H_2O molecules with Zr. In the absence of simulations for Zr in the presence of bulk water, we briefly discuss recent work on the wetting of an fcc metal surface by water nanodroplets and its spreading behavior.

5.1. Corrosion of Zr

We have looked at the interaction of a Zr surface to exposure by oxygen and hydrogen. At 300 K, we find that hydrogen readily diffuses into the bulk, while oxygen atoms remain in the surface layer. The first structure in Fig. 7(a) is 1 ML of oxygen placed on FCC surface sites and 1 ML of hydrogen in octahedral sites between the surface layer and the next subsurface atomic layer. As Fig. 7(a) shows, the oxygen stays on the surface, while hydrogen diffuses into the bulk. In contrast, if we simulate hydrogen on the surface and oxygen in subsurface octahedral sites, Fig. 7(b), then the oxygen atoms remain immobile but now act as a diffusion barrier to hinder the penetration of hydrogen into the surface. Experimentally the diffusion of H through the oxide scale is enhanced by cracks and grain boundaries [56]. Our simulated structure does not contain defects or a readily accessible diffusion pathway for the timescales observed. Thus, the presence of a layer of oxygen prohibiting hydrogen diffusion in COMB is not inconsistent with experiment.

For H_2O deposition, the rate of dissociation of a single water molecule is dependent on the surface structure. Fig. 8 shows a close-up view of a water molecule dissociating after 10 ps. Atomic oxygen diffuses into the bulk while atomic hydrogen diffuses across the surface, which is characteristic for the $\text{Zr}(0001)$ surface.

5.2. Spreading rate of water on Cu surfaces

In the absence of simulations of bulk molecular water in nuclear environments, we illustrate the capabilities of the COMB

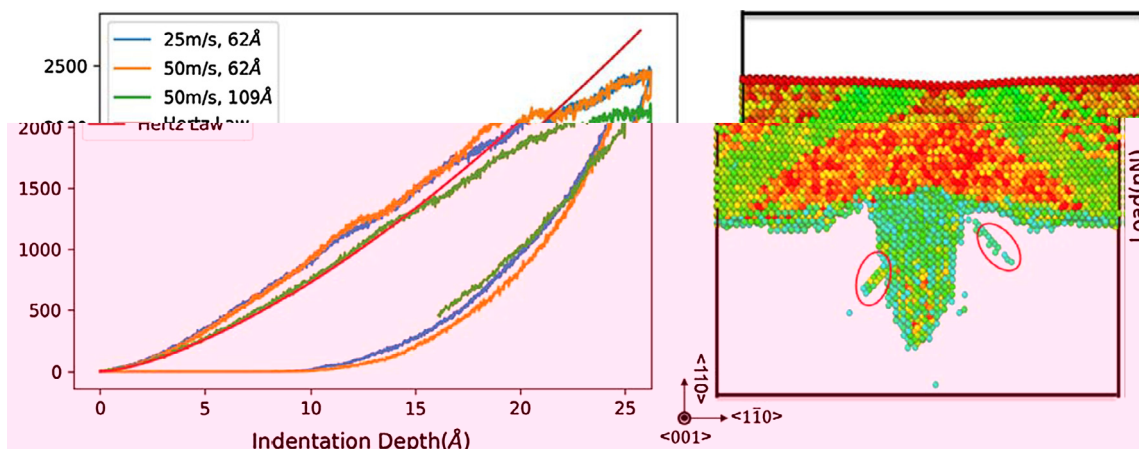


Fig. 6. (a) Theoretical load-displacement curve per the Hertz Law in red and load-displacement curves of indented ZrH_2 layers with different indenter speeds and active layer thicknesses in blue, orange and green. (b) The deformed structure at 16 Å indentation depth. The color of atoms represents the degree of disorder, with red indicating high disorder and green indicating low disorder. H atoms and Zr atoms whose CS parameter are lower than 3 are removed from the image. Dislocation loops along the $\langle 110 \rangle$ directions indicated with red ovals.

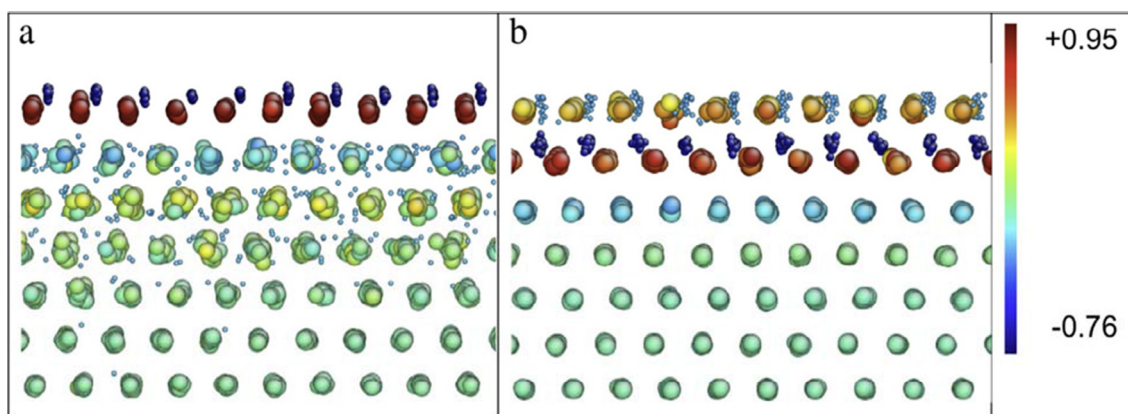


Fig. 7. Snapshot of Zr (0001) surface viewed along the $[11_20]$ direction after 50 ps at 300 K. Atoms are color-coded by charge. (a) Initial sites are surface FCC for oxygen and subsurface Octa(1, 2) for hydrogen. (b) Initial sites are surface FCC for hydrogen and subsurface Octa(1, 2) for oxygen. From Noordhoek [28].

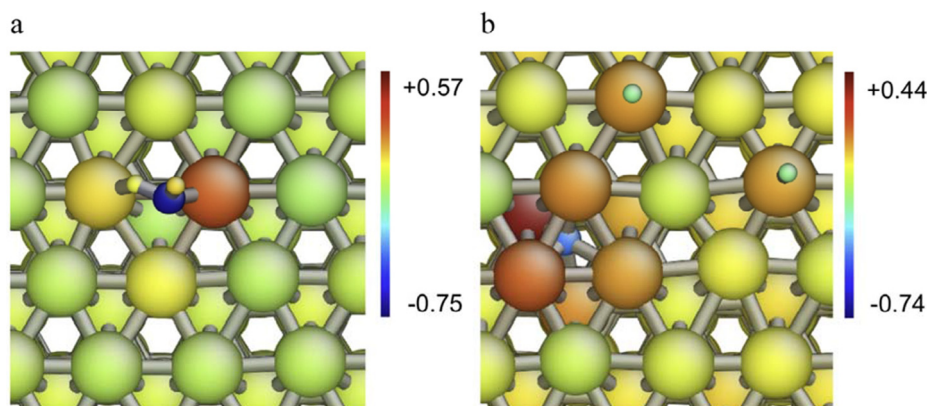


Fig. 8. (a) An H_2O molecule on $\text{Zr}(0001)$ and (b) after 10 ps the H_2O molecule has dissociated into atomic oxygen and hydrogen. The oxygen diffuses into the bulk while hydrogen remains adsorbed atop Zr surface atoms. The atoms are color coded by their charge.

formalism in another metallic system. Molecular water adsorbs on face centered cubic (fcc) transition metal surfaces such as Cu and Pt [57]. When considering H_2O molecules as bulk liquid or ice, hydrogen bonds exist between H atoms and O atoms in neighboring molecules. If liquid water in the form of a droplet or thin multilayer water film encounters a Cu or Pt surface, there is

now an energetic competition between molecules adsorbing at the surface and remaining in their hydrogen-bonded environment. Here, we briefly consider the interaction of water droplets on clean and chemically altered $\text{Cu}(111)$ and analyze how pre-adsorbed species affect the degree to which a droplet will spread across the surface.

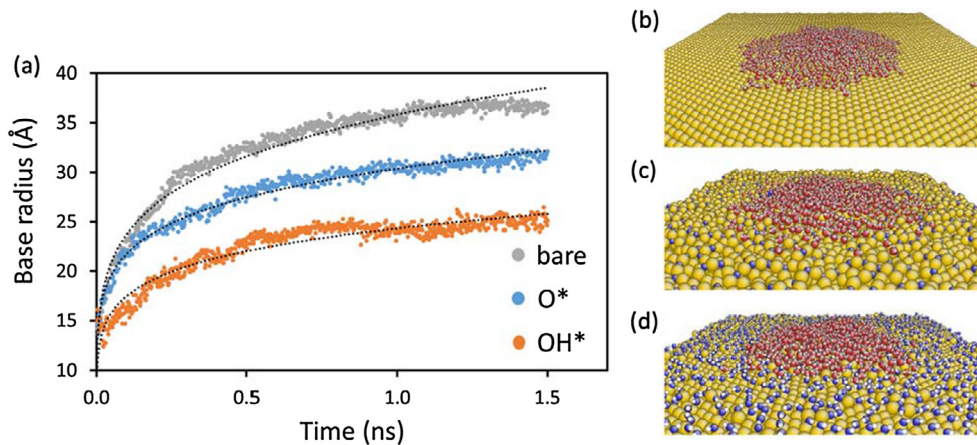


Fig. 9. (a) Spreading rates of water droplets on single crystal Cu(1 1 1) surface (bare) and 0.50 ML O* and OH* covered Cu(1 1 1). Snapshots after 1.5 ns of simulation time are shown for (b) Cu(1 1 1), (c) Cu(1 1 1)-O*, and (d) Cu(1 1 1)-OH*. Red atoms are O from H₂O, blue atoms are O from O* or OH*, and yellow atoms are Cu. From Antony et al. [32]. (For interpretation of the references to colour in this figure legend, the reader is referred to the web version of this article.)

In MD simulations, the spreading rate of a water nanodroplet is determined by monitoring the change in effective base radius, R_b , as a function of time. From COMB3 simulations of a droplet on Cu(1 1 1) under ambient conditions, initial spreading of the base radius is dictated by diffusion and subsequent adsorption of water molecules from the top of the droplet to the Cu surface near the advancing droplet front (i.e., the molecularly thin precursor film). A plot of spreading rates for water droplets on bare, O*, and OH* Cu(1 1 1) is shown in Fig. 9 [32]. After sufficient molecules have adsorbed onto the surface near the precursor film, the spreading rate is limited by the diffusion of molecules across the surface. As such, an eventual decrease in spreading rate after ~ 0.2 ns of simulation time is the result of slower diffusion across the surface compared to initial diffusion along the outer edge of the droplet.

From Fig. 9, the final base radius after 1.5 ns of simulation time for bare, O*, and OH* Cu(1 1 1) surfaces are 3.6 nm, 3.0 nm, and 2.4 nm, respectively. In the case of bare Cu(1 1 1), the droplet spreads at a rate of $R \sim t^{0.18}$ but for both O* and OH* covered Cu(1 1 1), the droplet exhibits a spreading rate of $R \sim t^{0.14}$. These results are consistent with previous MD studies which find that decreasing the wettability of a surface also reduces the rate at which the droplet spreads [58]. The underlying mechanism for the decrease in spreading rate is attributed to “pinning” effects at the chemically altered surface. As H₂O molecules from the droplet encounter chemical species at the surface, they become pinned between O* and OH*, reducing diffusion across the surface. Temporarily stable hydrogen bonds between H₂O molecules and O* and OH* species also contribute to the reduction in spreading rate.

6. Assessment of materials fidelity of COMB potentials

The ability of COMB potentials to be used for finite-temperature, time-dependent simulations of complex microstructures comes with two principal costs. First, as mentioned above, simulations with COMB potentials are ~ 100 times slower than those with EAM potentials (though orders of magnitude faster than equivalent DFT-MD simulations, when they are even possible). Second, as for all empirical potentials used in MD, the materials fidelity is generally not as high as that of DFT calculations. To illustrate one case in which the COMB potential shows high materials fidelity in some properties and somewhat compromised fidelity in others, we take the case of the Zr-H potential for the description of the ZrH_x system.

One critical but open question during hydride formation in Zr alloys is the nucleation mechanism of face-centered hydride

phases, including face-center-tetragonal (fct) γ (ZrH, $c > a$) and ε (ZrH₂ $c < a$), and face-centered-cubic (fcc) δ phase (ZrH_{1.5}). The δ phase has been widely observed in fuel claddings of light water reactors and, because it causes embrittlement, is a concern with regards to fuel integrity [59]. The most plausible theory is that the δ phase forms from γ , which forms from coherent clusters or hydride phases such as the ξ phase (Zr₂H) [60–62]. However, this theory has not been confirmed by experiments or observed in atomic scale simulations until recently by the present authors using the COMB potential for Zr-H systems [29]. To simulate the transition of hydride phases embedded in a Zr matrix requires a potential capable of describing H solution and various hydride phases. The potential needs to predict the right trend regarding the energetic trend in these phases. The COMB potential was found to serve this purpose well. Indeed, a thermodynamic pathway is predicted from H solution to ξ and then γ phase, as shown in Fig. 10.

Moreover, the COMB potential has also predicted a transformation path from ξ to γ phase (or ξ' , fct Zr₂H) with negligible barrier. This suggests a formation path of γ hydride: from H solution to ξ to ξ' , which will further grow into γ by absorbing more H atoms. Consistent with previous hypothesis, the transformation is via $(0\ 1\ \bar{1}\ 0)/3$ shear in the basal plane. Note that in the basal plane of hcp there exist three equivalent $(0\ 1\ \bar{1}\ 0)/3$ shear partials. These three partials can operate simultaneously during the transformation from ξ to γ . Consequently, the transformation can be accomplished without changing the hydride shape, minimizing the shear strain induced by the transformation. This process is similar to the twinning in fcc metals [63]. The mechanism identified from the atomistic simulations resolves the difficulty in the previous hypothesis, which is based on single shear and thus involves extremely high shear strain [60]. The COMB potential also predicts a negligible barrier needed to shear from ξ to γ , consistent with previous DFT calculations and experimental observations that hydride can form at relatively low temperatures without any mechanical loading.

Along with the valuable insight obtained, a few deficiencies of the COMB potential have also been identified. First, all the face-centered hydride phases are predicted to be fcc, while both ξ and γ should be fct. For γ the ordering of H atoms in $\{1\ 1\ 0\}$ planes is still correctly predicted. However, the martensitic transformation between γ and δ and that between δ to ε may not be represented correctly. Second, the magnitude of H solution energy of H is substantially overestimated for the tetrahedron site, -1.28 eV by COMB, in reference to -0.43 to 0.60 eV from DFT calculations [64–69] and -0.66 eV from experiments [70]. On the other hand,

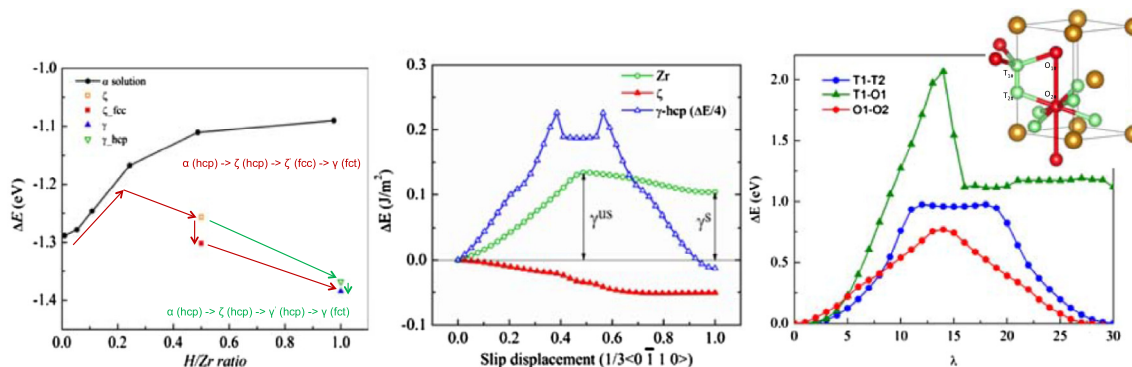


Fig. 10. (from left to right) (a) Formation energies of H solid solution and hydride phase as functions of H/Zr ratio, (b) general stacking fault energy surface shown by excess energy with respect to shear displacement, and (c) H diffusion barriers shown by excess energy with respect to the diffusion length. In (c) the total diffusion length is evenly divided into 30 images along the diffusion path for nudged-elastic-band calculations. (a) and (b) are from Zhang et al. [29].

the stability of H solution at the octahedron site is substantially underestimated, with a solution energy of -0.17 eV against the results of 0.37 – 0.53 eV from DFT. More precisely, the octahedron site is not stable and the H atom relaxes to a position slightly away from the octahedron site. Related to the solution energy, the COMB potential shows a poor performance in predicting the diffusion barriers and path of H in Zr. Considering the contribution of zero-point energy, the octahedron and tetrahedron sites are nearly equivalent energetically for H solution. Both sites are involved for long-range H diffusion, which is via first nearest neighbor T-T, T-O, O-O and O-T jumps. The corresponding barriers predicted by COMB are 0.976 eV, 2.067 eV, and 0.77 eV for T-T, T-O, and O-T jumps using the nudged-elastic-band method [Zhang, unpublished] (see Fig. 10(c)), comparing to 0.129 eV, 0.406 eV, and 0.398 eV from DFT calculations [69]. The discrepancy is significant enough to exclude using the current version of the COMB Zr-H potential for hydrogen diffusion. In addition to these major flaws, it needs to be pointed out that the generalized stacking fault energy surfaces in Zr and coherent ζ phase also differ from DFT calculations in terms of exact numbers. A current effort is being made to improve the COMB Zr-H potential to address the above issues.

Although the above analysis indicates limitations in the materials fidelity of the COMB potential, it is to be noted that all classical interatomic potentials make compromises in fidelity for the sake of computational speed and tractability.

7. Conclusions and outlook

The development of descriptions of empirical approaches that can describe different bonding types within the same simulation, such as COMB [11,5] and ReaxFF [8] has opened up new avenues to addressing important issues in materials behavior. Here we have focused only on applications of the COMB approach to nuclear fuel. In this context, we have seen that can address questions in both the fuel pellet itself and in the clad. Indeed, the above examples illustrate the capabilities of the COMB formalism to address a number of problems in nuclear materials. This includes both being able to provide atomic-level information on the atomic-level mechanisms associated important physical and chemical processes, and the ability to quantify the energetics and kinetics of such processes. Moreover, this information can then act as essential input to higher length scale models [2].

There are a large number of further fuel-related issues that the COMB approach could address, such as an extensive analysis of fission products and fuel-clad chemical interaction, but to which it has not yet been applied. The reason for this is that the potential parameters have not yet been developed. Such potential

parameterization is still more of an art than a science, though we have developed somewhat systematic approaches [71] and associated optimization software [72].

Acknowledgements

We are happy to acknowledge the contributions of our collaborators on the work reviewed here, particularly Yangzhong Li, Mark Noordhoek, Zizhe Lu, and Aleksandr Chernatynskiy. The work of SRP was supported by a DOE NEUP Award (DENE0000731). The work of MLF, YZ and SBB was supported by INL LDRDs 14-026 and 16-013. TL and SBS gratefully acknowledge the support of the National Science Foundation CBET-1264173. Computing resources at both University of Florida and Pennsylvania State University were utilized for this work.

Appendix A. Supplementary material

Supplementary data associated with this article can be found, in the online version, at <https://doi.org/10.1016/j.commatsci.2018.02.041>.

References

- [1] G.A. Berna, C.A. Beyer, K.L. Davis, D.D. Lanning, FRAPCON 3: a computer code for the calculation of steady-state, thermal-mechanical behavior of oxide fuel rods for high burnup, 1997.
- [2] M.R. Tonks, D. Andersson, S.R. Phillpot, Y. Zhang, R. Williamson, C.R. Stanek, B. P. Uberuaga, S.I. Hayes, Mechanistic materials modeling for nuclear fuel performance, *Ann. Nucl. Technol.* 105 (2017) 11–24, <https://doi.org/10.1016/j.anucene.2017.03.005>.
- [3] S.R. Phillpot, S.B. Sinnott, Simulating multifunctional nanostructures, *Science* (80–). 325 (2009) 1634–1635, <https://doi.org/10.1126/science.1177794>.
- [4] D.W. Brenner, Relationship between embedded-atom method and Tersoff potentials, *Phys. Rev. B.* 63 (1989) 1022, <https://doi.org/10.1103/PhysRevLett.63.1022>.
- [5] T. Liang, T.-R. Shan, Y.-T. Cheng, B.D. Devine, M.J. Noordhoek, Y. Li, Z. Lu, S.R. Phillpot, S.B. Sinnott, Classical atomistic simulations of surfaces and heterogeneous interfaces with the charge-optimized many body (COMB) potentials, *Mater. Sci. Eng. R* 74 (2013) 255–279, <https://doi.org/10.1016/j.mser.2013.07.001>.
- [6] T. Liang, Y.K. Shin, Y.-T. Cheng, D.E. Yilmaz, K.G. Vishnu, O. Veners, C. Zou, S.R. Phillpot, S.B. Sinnott, A.C.T. van Duin, Reactive potentials for advanced atomistic simulations, *Annu. Rev. Mater. Res.* 43 (2013) 109–129, <https://doi.org/10.1146/annurev-matsci-071312-121610>.
- [7] Y.K. Shin, T.-R. Shan, T. Liang, M.J. Noordhoek, S.B. Sinnott, A.C.T. van Duin, S.R. Phillpot, Variable charge many body interatomic potentials, *MRS Bull.* 37 (2012) 504–512, <https://doi.org/10.1557/mrs.2012.95>.
- [8] A.C.T. van Duin, S. Dasgupta, F. Lorant, W.A. Goddard III, ReaxFF: a reactive force field for hydrocarbons, *J. Phys. Chem. A* 2 (105) (2001) 9396–9409, <https://doi.org/10.1021/jp004368u>.
- [9] A.K. Rappe, W.A. Goddard III, Charge equilibration for molecular dynamics simulations, *J. Phys. Chem.* 93 (1991) 3358–3363.

- [10] J. Yu, S.B. Sinnott, S.R. Phillpot, Charge-optimized many body (COMB) potential for the Si/SiO₂ system, *Phys. Rev. B* 75 (2007) 85311, <https://doi.org/10.1103/PhysRevB.75.085311>.
- [11] J. Yu, S.R. Phillpot, S.B. Sinnott, Interatomic potential for the structure and energetics of tetrahedrally coordinated silica polymorphs, *Phys. Rev. B* 75 (2007) 233203, <https://doi.org/10.1103/PhysRevB.75.233203>.
- [12] T.-R. Shan, B.D. Devine, J.M. Hawkins, A. Asthagiri, S.R. Phillpot, S.B. Sinnott, Second generation charge-optimized many-body potential for Si/SiO₂ and amorphous silica, *Phys. Rev. B* 82 (2010) 235302, <https://doi.org/10.1103/PhysRevB.82.235302>.
- [13] J. Yu, S.B. Sinnott, S.R. Phillpot, Optimized many body potentials for fcc metals, *Philos. Mag. Lett.* 89 (2009) 136–144, <https://doi.org/10.1080/09500830802684114>.
- [14] T.-R. Shan, B.D. Devine, S.R. Phillpot, S.B. Sinnott, Molecular dynamics study of the adhesion of Cu/SiO₂ interfaces using a variable charge interatomic potential, *Phys. Rev. B* 83 (2011) 115327, <https://doi.org/10.1103/PhysRevB.83.115327>.
- [15] B.D. Devine, T.-R. Shan, Y.-T. Cheng, A.J.H. McGaughey, M. Lee, S.R. Phillpot, S.B. Sinnott, Atomistic simulations of copper oxidation and Cu/Cu₂O interfaces using charge-optimized many body potentials, *Phys. Rev. B* 84 (2011) 125308, <https://doi.org/10.1103/PhysRevB.84.125308>.
- [16] T.-R. Shan, B.D. Devine, T.W. Kemper, S.B. Sinnott, S.R. Phillpot, Charge-optimized many-body potential for the hafnium/hafnium oxide system, *Phys. Rev. B* 81 (2010) 125328, <https://doi.org/10.1103/PhysRevB.81.125328>.
- [17] Y.-T. Cheng, T.-R. Shan, B.D. Devine, D. Lee, T. Liang, B.B. Hinojosa, S.R. Phillpot, A. Asthagiri, S.B. Sinnott, Atomistic simulations of the adsorption and migration barriers of Cu adatoms on ZnO surfaces using COMB potentials, *Surf. Sci.* 606 (2012) 1280–1288, <https://doi.org/10.1016/j.susc.2012.04.007>.
- [18] Y.-T. Cheng, T. Liang, X. Nie, K. Choudhary, S.R. Phillpot, A. Asthagiri, S.B. Sinnott, Cu cluster deposition on Zn (10–10): morphology and growth mode predicted by molecular dynamics simulations, *Surf. Sci.* 621 (2014) 109–116, <https://doi.org/10.1016/j.susc.2013.10.025>.
- [19] T. Liang, B.D. Devine, S.R. Phillpot, S.B. Sinnott, Variable charge reactive potential for hydrocarbons to simulate organic-copper interactions, *J. Phys. Chem. A* 116 (2012) 7976–7991, <https://doi.org/10.1021/jp212083t>.
- [20] T. Liang, Y.-T. Cheng, X. Nie, W. Luo, A. Asthagiri, M.J. Janik, E. Andrews, J. Flake, S.B. Sinnott, Molecular dynamics simulations of CO₂ reduction on Cu(111) and Cu/Zn(10–10) using charge optimized many body potentials, *Catal. Commun.* 52 (2014) 84–87, <https://doi.org/10.1016/j.catcom.2013.11.033>.
- [21] Y. Li, T.-R. Shan, T. Liang, S.B. Sinnott, S.R. Phillpot, Classical interatomic potential for orthorhombic uranium, *J. Phys. Condens. Matter* 24 (2012) 235403, <https://doi.org/10.1088/0953-8984/24/23/235403>.
- [22] Y. Li, T. Liang, S.B. Sinnott, S.R. Phillpot, A charge-optimized many body potential for the U-UO₂-O₂ system, *J. Phys. Condens. Matter* 25 (2013) 505401, <https://doi.org/10.1088/0953-8984/25/50/505401>.
- [23] Y. Li, A. Chernatynskiy, J.R. Kennedy, S.B. Sinnott, S.R. Phillpot, Lattice expansion by intrinsic defects in uranium by molecular dynamics simulation, *J. Nucl. Mater.* 475 (2016) 6–18, <https://doi.org/10.1016/j.jnucmat.2016.03.018>.
- [24] Y.-T. Cheng, T.-R. Shan, T. Liang, R.K. Behera, S.R. Phillpot, S.B. Sinnott, A charge optimized many body (COMB) potential for titanium and titania, *J. Phys. Condens. Matter* 26 (2014) 315007, <https://doi.org/10.1088/0953-8984/26/31/315007>.
- [25] Y.-T. Cheng, T. Liang, J.A. Martinez, S.R. Phillpot, S.B. Sinnott, A charge-optimized many body potentials for titanium nitride (TiN), *J. Phys. Condens. Matter* 26 (2014) 265004, <https://doi.org/10.1088/0953-8984/26/26/265004>.
- [26] T. Liang, M. Ashton, K. Choudhary, D. Zhang, A.F. Fonseca, B.C. Revard, R.G. Hennig, S.R. Phillpot, S.B. Sinnott, Properties of Ti/TiC interfaces from molecular dynamics simulations, *J. Phys. Chem. C* 120 (2016) 12530–12538, <https://doi.org/10.1021/acs.jpcc.6b02763>.
- [27] M.J. Noordhoek, T. Liang, Z. Lu, T.-R. Shan, S.B. Sinnott, S.R. Phillpot, Charge optimized many body (COMB) potential for zirconium, *J. Nucl. Mater.* 441 (2013) 274–279, <https://doi.org/10.1016/j.jnucmat.2013.06.004>.
- [28] M.J. Noordhoek, T. Liang, T.-W. Chiang, S.B. Sinnott, S.R. Phillpot, Mechanisms of Zr surface corrosion via molecular dynamics simulations with charge optimized many body (COMB) potentials, *J. Nucl. Mater.* 452 (2014) 285–295, <https://doi.org/10.1016/j.jnucmat.2014.05.023>.
- [29] Y. Zhang, X.-M. Bai, J. Yu, M.R. Tonks, M.J. Noordhoek, S.R. Phillpot, Homogeneous hydride formation path in a-Zr: molecular dynamics simulations with the charge-optimized many-body potential, *Acta Mater.* 111 (2016) 357–365, <https://doi.org/10.1016/j.actamat.2016.03.079>.
- [30] A. Kumar, A. Chernatynskiy, T. Liang, K. Choudhary, M.J. Noordhoek, Y.-T. Cheng, S.R. Phillpot, S.B. Sinnott, Charge optimized many body (COMB) potential for dynamical simulation of Ni-Al phases, *J. Phys. Condens. Matter* 27 (2015) 336302, <https://doi.org/10.1088/0953-8984/27/33/336302>.
- [31] A. Kumar, A. Chernatynskiy, T. Liang, K. Choudhary, M.J. Noordhoek, Y.-T. Cheng, S.R. Phillpot, S.B. Sinnott, Corrigendum: charge optimized many body potentials for dynamics simulation of Ni-AL phases, *J. Phys. Condens. Matter* 27 (2015) 479501, <https://doi.org/10.1088/0953-8984/27/47/479501>.
- [32] A.C. Antony, T. Liang, S.A. Akhade, M.J. Janik, S.R. Phillpot, S.B. Sinnott, Effect of surface chemistry on water interaction with Cu (111), *Langmuir* 32 (2016) 8061–8070, <https://doi.org/10.1021/acs.langmuir.6b01974>.
- [33] K. Choudhary, T. Liang, K. Mathew, B.C. Revard, A. Chernatynskiy, S.R. Phillpot, R.G. Hennig, S.B. Sinnott, Dynamics properties of AlN nanostructures and heterogeneous interfaces predicted using COMB potentials, *Comput. Mater. Sci.* 113 (2016) 80–87, <https://doi.org/10.1016/j.commatsci.2015.11.025>.
- [34] K. Choudhary, T. Liang, A. Chernatynskiy, S.R. Phillpot, S.B. Sinnott, Charge optimized many-body (COMB) potential for Al₂O₃ materials, interfaces and nanostructures, *J. Phys. Condens. Matter* 27 (2015) 305004, <https://doi.org/10.1088/0953-8984/27/30/305004>.
- [35] A.C. Antony, S.A. Akhade, Z. Lu, T. Liang, M.J. Janik, S.R. Phillpot, S.B. Sinnott, Charge optimized many body (COMB) potentials for Pt and Au, *J. Phys. Condens. Matter* 29 (2017) 225901, <https://doi.org/10.1088/1361-648X/aa6d43>.
- [36] J.A. Martinez, T. Liang, S.B. Sinnott, S.R. Phillpot, A third-generation charge optimized many body (COMB) potential for nitrogen-containing organic molecules, *Comput. Mater. Sci.* 139 (2017) 153–161, <https://doi.org/10.1016/j.commatsci.2017.07.019>.
- [37] D.E. Smirnova, S.V. Starikov, V.V. Stegailov, Interatomic potential for uranium in a wide range of pressures and temperatures, *J. Phys. Condens. Matter* 24 (2012) 15702, <https://doi.org/10.1088/0953-8984/24/1/015702>.
- [38] M.I. Pascuet, G. Bonny, J.R. Fernandez, Many-body interatomic U and Al-U potentials, *J. Nucl. Mater.* 424 (2012) 158–163, <https://doi.org/10.1016/j.jnucmat.2012.03.002>.
- [39] Y. Dai, C.H. Lu, Q.B. Ren, L. Lu, J.H. Li, B.X. Liu, A long-range U-Nb potential for the calculations of some chemical and physical properties of the U-Nb system, *J. Nucl. Mater.* 427 (2012) 239–244, <https://doi.org/10.1016/j.jnucmat.2012.05.008>.
- [40] J.R. Fernandez, M.I. Pascuet, On the accurate description of uranium metallic phases: a MEAM interatomic potentials approach, *Model. Simul. Mater. Sci. Eng.* 22 (2014) 55019, <https://doi.org/10.1088/0965-0393/22/5/055019>.
- [41] J. Sugar, Ionization energies of neutral actinides, *J. Chem. Phys.* 59 (1973) 788–791, <https://doi.org/10.1063/1.1680874>.
- [42] B. Hudson, The distribution of and swelling produced by fission gas bubbles in a and b uranium irradiated under low stress, *J. Nucl. Mater.* 22 (1967) 121–136.
- [43] C.D. Taylor, Evaluation of first-principles techniques for obtaining materials parameters for a-uranium and the (001) a-uranium surface, *Phys. Rev. B* 77 (2008) 94119, <https://doi.org/10.1103/PhysRevB.77.094119>.
- [44] K. Govers, S. Lemehov, M. Hou, M. Verwerf, Comparison of interatomic potentials for UO₂, Part I: static calculations, *J. Nucl. Mater.* 366 (2007) 161–177, <https://doi.org/10.1016/j.jnucmat.2006.12.070>.
- [45] K. Govers, S. Lemehov, M. Hou, M. Verwerf, Comparison of interatomic potentials for UO₂, Part II: molecular dynamics simulations, *J. Nucl. Mater.* 376 (2008) 66–77, <https://doi.org/10.1016/j.jnucmat.2008.01.023>.
- [46] A. Chernatynskiy, C. Flint, S.B. Sinnott, S.R. Phillpot, Critical assessment of UO₂ classical potentials for thermal conductivity calculations, *J. Mater. Sci.* 47 (2012) 7693–7702, <https://doi.org/10.1007/s10853-011-6230-0>.
- [47] G. Sattouy, R. Tetot, Bulk, surface and point defects in UO₂ from a tight-binding variable-charge model, *J. Phys. Condens. Matter* 25 (2013) 125403, <https://doi.org/10.1088/0953-8984/25/12/125403>.
- [48] D.R. Olander, *Fundamental Aspects of Nuclear Reactor Fuel Elements*, University of California, Berkeley, Berkeley, CA, 1976, <http://www.osti.gov/scitech/biblio/7343826>.
- [49] A.S. Clarke, H. Jonsson, Structural changes accompanying densification of random hard-sphere packings, *Phys. Rev. E* 47 (1993) 3975–3984, <https://doi.org/10.1103/PhysRevE.47.3975>.
- [50] H. Jonsson, H. Andersen, Icosahedral ordering in Lennard-Jones liquid and glass, *Phys. Rev. Lett.* 60 (1988) 2295–2298.
- [51] Z. Lu, A. Chernatynskiy, M.J. Noordhoek, S.B. Sinnott, S.R. Phillpot, Nanoindentation of Zr by molecular dynamics simulation, *J. Nucl. Mater.* 467 (2015) 742–757, <https://doi.org/10.1016/j.jnucmat.2015.10.042>.
- [52] Z. Lu, A. Chernatynskiy, M.J. Noordhoek, S.B. Sinnott, S.R. Phillpot, Nanoindentation of ZrO₂ and ZrO₂/Zr systems by molecular dynamics simulation, *J. Nucl. Mater.* 486 (2017) 250–266, <https://doi.org/10.1016/j.jnucmat.2017.01.022>.
- [53] M.P. Puls, *The Effect of Hydrogen and Hydrides on the Integrity of Zirconium Alloy Components*, Springer, 2012.
- [54] A.T. Motta, L.Q. Chen, Hydride formation in zirconium alloys, *JOM* 64 (2012) 1403, <https://doi.org/10.1007/s11837-012-0479-x>.
- [55] C.L. Kelchner, S.J. Plimpton, J.C. Hamilton, Dislocation nucleation and defect structure during surface indentation, *Phys. Rev. B* 58 (1998) 11085–11088.
- [56] M. Grosse, E. Lehmann, M. Steinbrück, G. Kuhne, J. Stuckert, Influence of oxide layer morphology on hydrogen concentration in tin and niobium containing zirconium alloys after high temperature steam oxidation, *J. Nucl. Mater.* 385 (2009) 339–345, <https://doi.org/10.1016/j.jnucmat.2008.12.021>.
- [57] A. Michaelides, V.A. Ranea, P.L. de Andros, D.A. King, General model for water monomer adsorption on close-packed transition and noble metal surfaces, *Phys. Rev. Lett.* 90 (2003) 216102.
- [58] N. Sedighi, S. Murad, S.K. Aggarwal, Molecular dynamics simulations of spontaneous spreading of a nanodroplet on solid surfaces, *Fluid Dyn. Res.* 43 (2011) 15507.
- [59] T.R. Allen, R.J.M. Konings, A.T. Motta, *Corrosion of Zirconium Alloys*, in: R.J.M. Konings (Ed.), *Compr. Nucl. Mater.*, Elsevier, Amsterdam, 2012, pp. 49–68.
- [60] G.J.C. Carpenter, The precipitation of gamma-zirconium hydride in zirconium, *Acta Mater.* 26 (1978) 1225.
- [61] L. Holliger, A. Legris, R. Besson, Hexagonal-based ordered phases in H-Zr, *Phys. Rev. B* 80 (2009) 94111.
- [62] Z. Zhao, J.P. Morniroli, A. Legris, A. Ambard, Y. Khin, L. Legras, M. Blat-Yrieix, Identification and characterization of a new zirconium hydride, *J. Microsc.* 232 (2008) 410.
- [63] Y.T. Zhu, X.Z. Liao, X.L. Wu, Deformation twinning in nanocrystalline materials, *Prog. Mater. Sci.* 1 (2012) 1–62.

- [64] C. Domain, R. Besson, A. Legris, Atomic-scale Ab-initio study of the Zr-H system: I. Bulk Properties, *Acta Mater.* 50 (2012) 3513.
- [65] M. Christensen, W. Wolf, C.M. Freeman, E. Wimmer, R.B. Adamson, L. Hallstadius, P.E. Cantonwine, E. Mader, H in α -Zr and in zirconium hydrides: solubility, effect on dimensional changes, and the role of defects, *J. Phys. Condens. Matter.* 27 (2015) 25402.
- [66] P.A. Burr, S.T. Murphy, S.C. Lumley, M.R. Wenman, R.W. Grimes, Hydrogen accommodation in Zr second phase particles: implications for H pick-up and hydriding of zircaloy2 and zircaloy4, *Corros. Sci.* 69 (2013) 1–4.
- [67] Y. Udagawa, M. Yamaguchi, H. Abe, N. Sekimura, T. Fuketa, Ab initio study on plane defects in zirconium-hydrogen solid solution and zirconium hydride, *Acta Mater.* 58 (2010).
- [68] S.C. Lumley, R.W. Grimes, S.T. Murphy, P.A. Burr, A. Choneos, P.R. Chard-Tuckey, M.R. Wenman, The thermodynamics of hydride precipitation: the importance of entropy, enthalpy and disorder, *Acta Mater.* 79 (2014) 351.
- [69] Y. Zhang, C. Jiang, X.-M. Bai, Anisotropic hydrogen diffusion in α -Zr and Zircaloy predicted by accelerated kinetic Monte Carlo simulations, *Sci. Rep.* 7 (2017) 41033.
- [70] E. Zuzek, J. Abriata, A. San-Martin, F. Manchester, The H-Zr (hydrogen-zirconium) system, *Bull. Alloy Phase Diagrams* 11 (1990) 385.
- [71] J.A. Martinez, D.E. Yilmaz, T. Liang, S.B. Sinnott, S.R. Phillpot, Fitting empirical potentials: challenges and methodologies, *Curr. Opin. Solid State Mater. Sci.* 17 (2013) 263–270, <https://doi.org/10.1016/j.cossms.2013.09.001>.
- [72] J.A. Martinez, A. Chernatynskiy, D.E. Yilmaz, T. Liang, S.B. Sinnott, S.R. Phillpot, Potential optimization software for materials (POSMat), *Comput. Phys. Commun.* 203 (2016) 201–211.